Journal of Materials Chemistry A

ROYAL SOCIETY OF CHEMISTRY

PAPER

View Article Online
View Journal | View Issue



Cite this: J. Mater. Chem. A, 2025, 13, 42118

# Solution-processed CuI as a hole transport layer for Sn–Pb perovskite solar cells

Riccardo Pau, [ab] David Garcia Romero, [a] Matteo Pitaro, [a] Lorenzo Di Mario, [a] Qianshan Feng,[a] Michele Saba [b] and Maria Antonietta Loi *[a]

Received 20th August 2025
Accepted 31st October 2025

DOI: 10.1039/d5ta06770g

rsc.li/materials-a

Mixed tin–lead (Sn–Pb) perovskites have received a lot of attention as active layers for both single-junction and tandem solar cells because of their optimal band gap. Generally, Sn–Pb perovskite solar cells are fabricated in a p–i–n structure using PEDOT:PSS as the hole transport layer (HTL), though its hygroscopic nature adversely affects the long-term stability of the perovskite layer. Here, we propose copper iodide (CuI), with high conductivity, wide bandgap, and optical transparency, as a low-cost and earth-abundant HTL candidate for Sn–Pb perovskite solar cells. Utilizing CuI as the HTL and an active layer composed of $EACl_{0.015}Cs_{0.25}FA_{0.75}Sn_{0.5}Pb_{0.5}I_3$ passivated with sodium fluoride (NaF), we obtained a remarkable short circuit current of 32.85 mA $cm^{-2}$ with a champion power conversion efficiency of 20.1%, while control devices with PEDOT:PSS showed an efficiency of 19.03% and a $J_{sc}$ value of 30.59 mA $cm^{-2}$. In addition, the implemented CuI layer improved the device stability when stored in $N_2$ and under thermal stress conditions at 85 °C.



## Introduction

Over the last years, the remarkable advancement in the power conversion efficiency of metal halide perovskites (MHP) in single-junction solar cells[1] has been accompanied by a growing apprehension regarding their environmental impact.[2] This concern primarily arises from the significant presence of water-soluble lead in the active material. To confront this challenge, tin (Sn)-based and mixed tin–lead (Sn–Pb)-based perovskites are sturdily emerging as promising substitutes for lead (Pb)-based compounds.[3,4] Furthermore, due to their smaller bandgap,[5,6] Sn and Sn–Pb perovskite materials play an obvious promising role in all-perovskite tandem devices with an efficiency that is expected to overcome 35%.[7–9]

However, this thriving solution presents new obstacles to surmount, such as the introduction of intrinsic Sn-defects and the easy oxidation of Sn(II) to Sn(IV), both of which contribute to the ongoing challenge of achieving competitive photovoltaic performances that remain, to date, considerably inferior to those exhibited by Pb-based perovskites.

The alloying of the Sn-based perovskite with Pb is considered as a strategy to partially overcome the difficulties of working with pure Sn, while decreasing the amount of Pb atoms in the active material by 50% compared to pure Pb-based perovskites. It is reported that the addition of Pb up to 50% stabilizes the perovskite, limiting the oxidation of Sn atoms[10,11] and reducing the achievable band gap.

The best Sn–Pb-based devices are currently fabricated in the p–i–n planar configuration since the n–i–p architecture faces significant obstacles as the Sn component is suspected to react with the most common ETLs, which are based on metal oxides.[12–14] Additionally, the energy level mismatch between the active material and the transport layers limits efficient charge extraction, resulting in a significant hysteresis and large energy loss in devices.[15]

In p–i–n perovskite solar cells, the choice of the hole transport layer (HTL) is of paramount importance to achieve high-performance solar cells. The extraction properties of this layer are generally considered together with their energy alignment with the active layer, and the transparency of this layer is of utmost importance as it maximizes the amount of light reaching the active layer; hence, directly impacting the power conversion efficiency. Furthermore, it is important to remember that the stability of the solar cell can be strongly influenced by the morphology and the mechanical and chemical properties of the HTL material.[16] Finally, foreseeing the commercialization of perovskite solar cells, the abundance and cost of the HTL material must be considered.

In the p–i–n configuration, PEDOT:PSS (poly(3,4-ethylenedioxythiophene)polystyrene sulfonate) is currently the most widely used hole transport layer.[17] However, the acidic and hygroscopic nature of this polymer is known to potentially limit the overall device stability over time and has been demonstrated to limit the efficiency, negatively impacting the crystallization of the perovskite active layer.[18–20]

[a]Zernike Institute for Advanced Materials, University of Groningen, Nijenborgh 3, 9747 AG, Groningen, The Netherlands. E-mail: M.A.Loi@rug.nl
[b]Dipartimento di Fisica, Università di Cagliari, 09042 Monserrato, Italy

At the current state-of-the-art, there are a limited number of materials that are suitable to replace PEDOT:PSS in Sn–Pb perovskite solar cells. In 2018, Shao *et al.*[18] demonstrated promising results by employing a pH neutral anionic conjugated polymer with alkylsulfonate side groups, PCP-Na. In addition to the improved power conversion efficiency, these devices also demonstrate enhanced reproducibility and stability compared to those utilizing PEDOT:PSS as the HTL.

Another organic material that garnered attention as the HTL for Sn–Pb perovskite solar cells is poly-[bis(4-phenyl) (2,4,6-trimethylphenyl)amine] (PTAA).[21] While PTAA offers high hole mobility and favourable energy alignment with the active material, its application is hindered by challenges such as poor reproducibility and high material costs, which have tempered enthusiasm within the research community.

In recent years, self-assembled monolayers (SAMs) based on a carbazole core have emerged as a promising new class of HTLs, starting with the prototypical molecule (2-(9*H*-carbazol-9-yl)ethyl)phosphonic acid (2PACz). Compared to PEDOT:PSS, SAMs show minimal parasitic absorption and low charge recombination but still face issues related to their hydrophobicity, which affects the scalability and reproducibility of perovskite layer deposition.[22,23]

Here, for the first time, we investigated the use of solution-processed copper iodide (CuI) as a hole transport layer in Sn/Pb-based perovskite solar cells. CuI is an earth-abundant and environmentally sustainable material that exhibits high electrical conductivity (>200 S cm$^{-1}$), a wide bandgap ($E_g = 3.1$ eV), and optical transparency across the visible spectrum,[24,25] making it an attractive low-cost candidate for large-area electronics and optoelectronics. Its use as a transparent conductor was first reported in 1907,[26,27] and since then, CuI thin films have been fabricated using a wide variety of techniques such as vapor iodization,[26] sputtering,[24] pulsed laser deposition,[28] liquid iodination[29] and solution-based depositions.[30–32]

While early studies demonstrated the use of the CuI HTL in Pb-based perovskite solar cells, they reported only modest improvements in terms of PCE and device stability, and for this reason, investigations stopped at an early stage.[33,34] To date, however, CuI has not been systematically explored in Sn-based or mixed Sn–Pb perovskite systems.

In this study, we present the application of CuI as a hole transport layer deposited from solution for the fabrication of

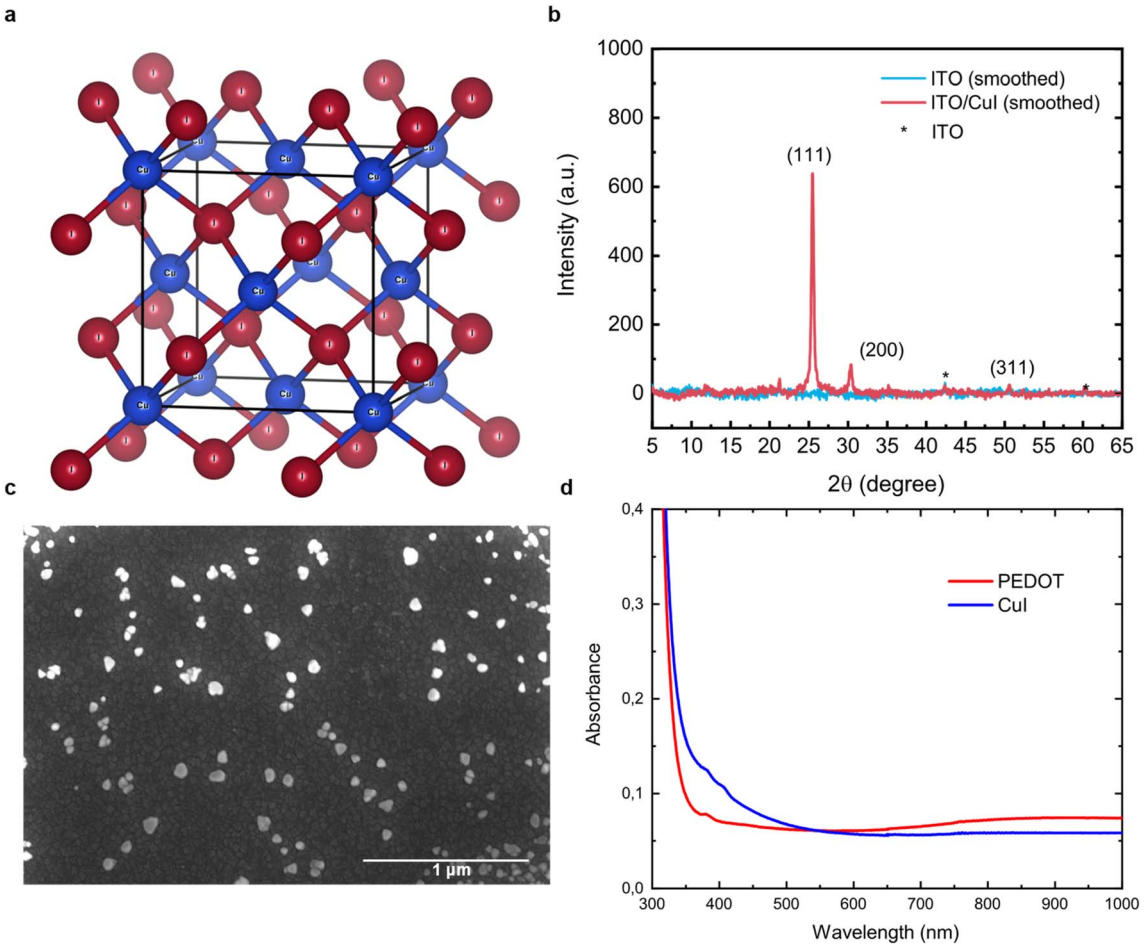


Fig. 1 (a) Schematic of the crystal structure of CuI. Cu and I atoms are represented in blue and red, respectively. (b) X-ray diffraction (XRD) patterns of CuI deposited on ITO glass substrates (red) and the reference ITO glass substrate (blue). (c) SEM image of the CuI film. (d) Absorbance spectra of PEDOT:PSS and CuI deposited on ITO.

methylammonium (MA)-free Sn–Pb perovskite solar cells. A champion device using CuI as the HTL reached a power conversion efficiency (PCE) of 20.1% with a remarkable short-circuit current ($J_{sc}$) of 32.85 mA cm$^{-2}$, while the champion reference device using PEDOT:PSS exhibited a PCE of 19.03% with a $J_{sc}$ value of 30.59 mA cm$^{-2}$. In addition, we demonstrated enhanced device stability under nitrogen storage and thermal stress conditions (85 °C), further underscoring the potential of CuI as a robust HTL in Sn-containing perovskite solar cells.

## Results and discussion

Fig. 1a shows the crystal structure of copper(I) iodide (CuI), the material investigated in this study as the HTL. Fig. 1b displays the X-ray diffraction (XRD) pattern of a spin-coated CuI thin film.

The observed diffraction peaks at $2\theta = 25.4°$, 30.3°, and 50.6° were indexed as represented in the graph to the (111), (200) and (311) planes of CuI, respectively, as they are in good agreement with the standard pattern of the γ-phase of CuI (Fig. S5), known to be the most stable form of the material at room temperature. The predominant (111) peak suggests a preferential orientation of the thin film grains along this plane.[24,35–37]

The corresponding scanning electron microscopy (SEM) and atomic force microscopy (AFM) micrographs in Fig. 1c and S1b, respectively, show the morphology of the solution-processed CuI film. The thin films appear as polycrystalline with a grain size in the order of 30 nm, with a surface texture composed of small islands of material. From our AFM micrographs, the CuI film surface has a root-mean-square (RMS) roughness of 7.8 ± 0.6 nm. For comparison, the bare ITO substrate shows an RMS roughness of 3.7 ± 0.8 nm, as presented in Fig. S1a. The morphology of CuI appears as formed by disconnected crystallites, leaving the underlying ITO morphology visible in some portions of the film (Fig. S1b), which is in agreement with previous reports.[30,34]

The absorbance spectra of PEDOT:PSS and CuI thin films, deposited on ITO substrates, are presented in Fig. 1d. While PEDOT:PSS exhibits lower absorbance at shorter wavelengths, CuI shows reduced absorption from 600 nm onward, extending into the spectral region where the bandgap of Sn–Pb-based perovskites is located.[22] Therefore, CuI could bring optical advantage when used with Sn–Pb perovskite active layers.

The growth of the perovskite active layer on the top of CuI was first studied through SEM imaging. The morphological results are reported in Fig. 2 and S4, in comparison with those of the perovskite growth on PEDOT:PSS. Larger perovskite grains, with an average of about 400 nm, are observed when the active layer is deposited on PEDOT:PSS, while the typical grain size is about 300 nm on the top of CuI. A difference in grain size results from the nucleation and crystallization process, which may result from variations in surface energy. To investigate this effect, we measured the contact angle of the perovskite precursor solution on each hole transport layer. The results revealed slightly better wetting on PEDOT:PSS, with a contact angle of approximately 10°, compared to 22° on CuI (Fig. S2). However, this modest variation in surface wettability does not compromise the overall film quality or uniformity. In fact, the perovskite formed on the top of PEDOT:PSS presents a higher number of pinholes located near the grain boundaries with respect to the perovskite grown on the top of CuI, in agreement with previous reports.[18,23] Such defects have been suggested to be the cause of undesired non-radiative recombination through the device (*vide infra*).

It has been reported that a DMF : DMSO mixture can damage the CuI layer due to its high solubility in these solvents.[38] To verify this effect, we performed AFM measurements on a CuI film after washing it with DMF : DMSO (4 : 1), which revealed

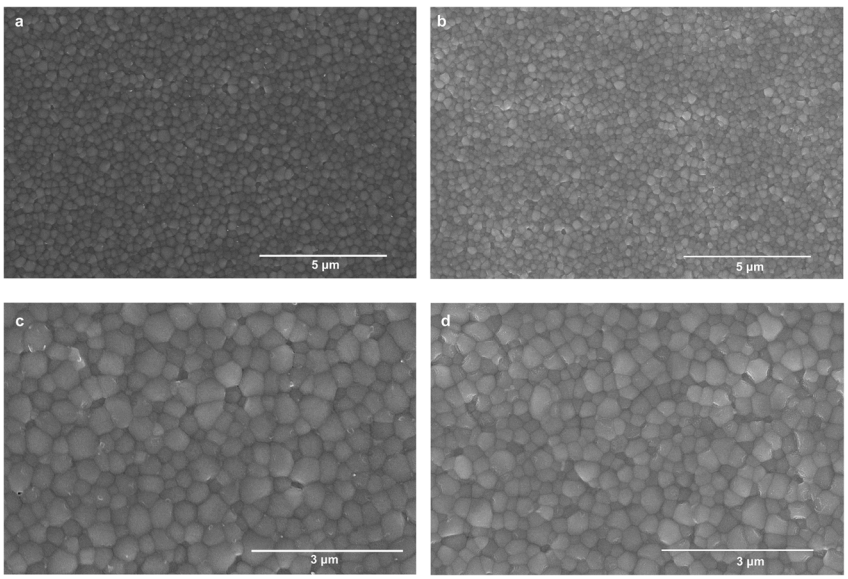


Fig. 2 SEM images of $EACl_{0.015}Cs_{0.25}FA_{0.75}Sn_{0.5}Pb_{0.5}I_3$ perovskite films deposited on top of PEDOT:PSS (a–c) and CuI (b–d) at larger (5 micron scale bar) and smaller (3 micron scale bar) magnifications, respectively.

 

partial dissolution of the CuI crystallites (Fig. S3). However, the situation changes when perovskite precursors are dissolved in the same solvent mixture. Contact angle measurements over time, performed using a perovskite precursor solution in DMF : DMSO (4 : 1) on CuI, revealed no measurable change in contact angle (Fig. S6b). This invariance in wetting behavior demonstrates that the CuI surface properties remain unaltered during exposure, providing direct evidence of its robustness under the processing conditions used in our study. For comparison, the same measurement was also carried out on PEDOT:PSS, and a comparable wetting dynamic was found.

Steady-state and time-resolved photoluminescence (PL) measurements were performed to further investigate the physical properties of the perovskite layer on the top of the two HTLs (Fig. S7 and S8). Comparing the two spectra, a slight redshift is observed in the CuI/perovskite film with respect to the PEDOT:PSS/perovskite one, which can indicate a higher doping concentration of the latter, related to the easier oxidation of tin in the active material and the well-known blue-shift.[39] The higher steady-state PL intensity and the longer average decay time (74 ns compared to 22 ns, Table S1) observed in time-resolved PL for the sample deposited on CuI suggest a reduction in non-radiative recombination, providing further evidence of a less-defective interface with the perovskite. It is important to note that the PL measurements were performed in the reflection mode, exciting the sample from the side of the substrate, meaning that, considering the very high absorption coefficient of the perovskite, the 400 nm excitation is absorbed in less than 100 nm at the interface with the HTL. Therefore, the PL and time-resolved PL measurements not only probe the quality of the perovskite but also an eventual charge transfer to the HTL and the interaction of the photoexcitations with defects at that interface.

The impact of CuI as the HTL, compared to PEDOT:PSS, was evaluated by fabricating solar cells with the architecture schematically shown in Fig. 3a, using $EACl_{0.015}Cs_{0.25}FA_{0.75}Sn_{0.5}Pb_{0.5}I_3$ as the active layer. The incorporation of the ethylammonium ($EA^+$) cation is known to enhance the tin-based perovskite film's morphology, stabilize its crystallization process, and improve the device performance.[40–42]

Fig. 3b shows the *JV* characteristics under AM1.5 illumination conditions for the best devices using each of the two HTL materials under study. The champion reference device, using PEDOT:PSS as the HTL, exhibits a power conversion efficiency (PCE) of 19.03%, with a short-circuit current ($J_{sc}$) of 30.59 mA $cm^{-2}$, an open-circuit voltage ($V_{oc}$) of 0.82 V, and a fill factor (FF) of 0.76. In comparison, devices using copper iodide as the HTL show a significant improvement in power conversion efficiency,

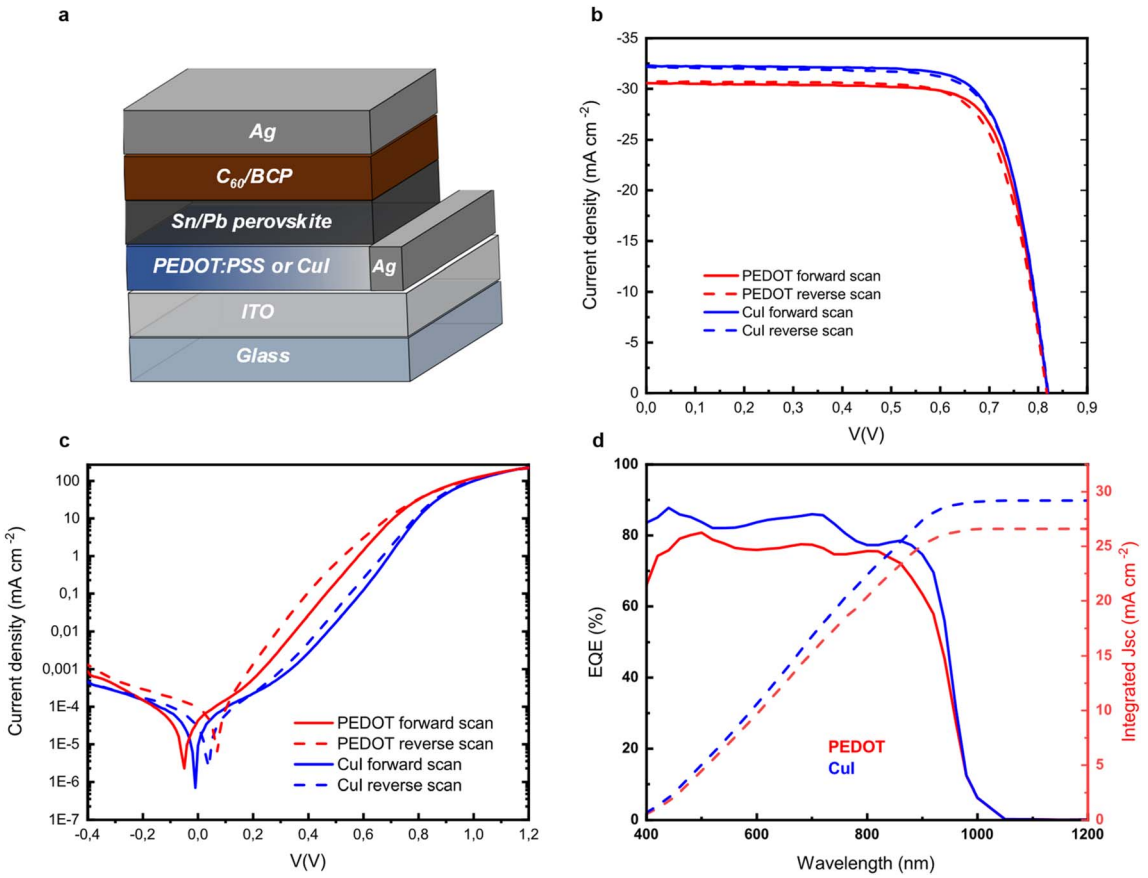


Fig. 3 (a) Device structure of the fabricated p–i–n perovskite solar cell. (b) Current density–voltage (*J*–*V*) and (c) dark *JV* curves of perovskite solar cells fabricated using PEDOT:PSS (red) and CuI (blue) as HTLs. (d) External quantum efficiency (EQE) as a function of wavelength and integrated current of the two different structures used.

with the device reaching a PCE of 20.10%, a $J_{sc}$ value of 32.85 mA cm$^{-2}$, a $V_{oc}$ value of 0.81 V, and an FF value of 0.75. The remarkable efficiency improvement was determined by the higher current achieved with a slightly lower open circuit voltage and FF.

To further investigate this improvement, we analyzed the *JV* characteristics under dark conditions for the two device architectures. The device fabricated on CuI presents a lower dark current density, which can be linked to a lower leakage due to the reduced density of pinholes in the active material previously mentioned. In addition, the sample fabricated on CuI presents a lower hysteresis between the forward and the reverse scan in the dark, which can be explained by a less defective interface and a smaller trapping activity in the dark. The external quantum efficiency (EQE) measurements confirm the current increase in the sample using CuI as the HTL compared to the one using PEDOT:PSS (Fig. 3d). Notably, the EQE is higher across all wavelengths for CuI, not just in the regions where its absorption is lower, as shown in the absorption spectra (Fig. 1d). This suggests that the improvement in $J_{sc}$ is driven not only by optical effects but also by the enhanced electrical properties of the transport layer.

It is important to note that the integrated current from the EQE and the $J_{sc}$ as measured from the *JV* characteristics shows a discrepancy of a few mA cm$^{-2}$ (precisely 3.99 for the reference sample and 3.65 for the CuI sample). This difference is attributed to the very different measurement conditions: while the EQE was measured using incident monochromatized light of around 50 μW without bias illumination, the *JV* measurements were performed under standard 1-sun illumination. Overall, this small discrepancy is not significant for the conclusions of our study. What is relevant, however, is that both measurements show the same trend between the two types of samples.

The statistical distribution of photovoltaic parameters over 20 devices per type, presented in Fig. 4, shows the good reproducibility of the perovskite solar cells under investigation and corroborates the trend exhibited by the two champion devices. The calculated average PCE of devices fabricated on PEDOT:PSS is 18.3% ± 0.4% while for the one fabricated on CuI is 19.4% ± 0.5%. It is clear that the drastic improvement in short-circuit current, which goes from 29.9 ± 0.8 mA cm$^{-2}$ for the reference device to 32.1 ± 0.4 mA cm$^{-2}$ for devices using CuI as the HTL, is mainly responsible for the improved PCE.

Within all devices fabricated, the average $V_{oc}$ for the reference devices and the ones using CuI are equal to 0.814 ± 0.010 V

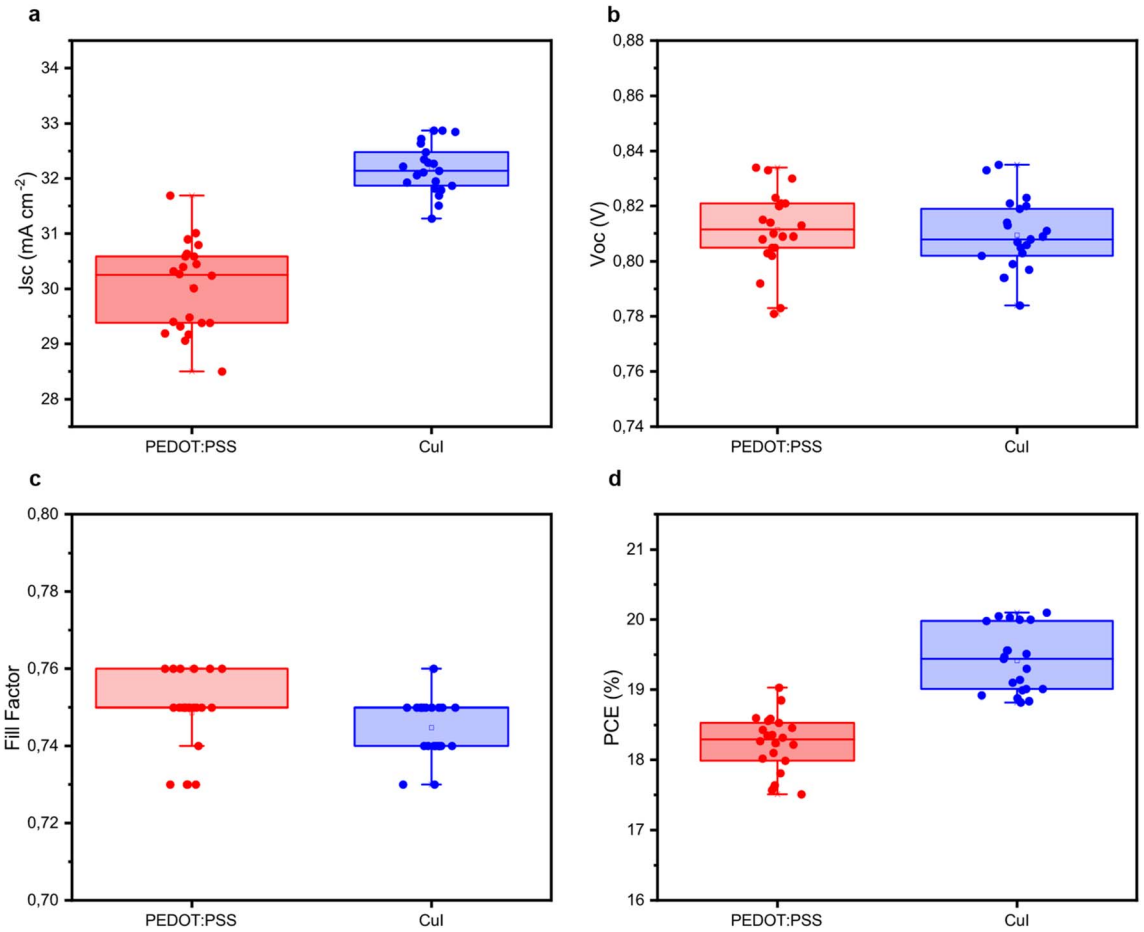


Fig. 4 Distribution of the photovoltaic parameters derived from the *JV* scans of the PEDOT:PSS (red) and CuI (blue) devices (the statistical overview is given based on 20 samples fabricated for every condition): (a) $J_{sc}$, (b) $V_{oc}$, (c) FF and (d) PCE.

 

and 0.811 ± 0.012 V, respectively, with a minor difference that lies within the statistical uncertainty (Fig. 4b). Similar values are also observed for the FF: 0.751 ± 0.009 for the reference devices and 0.750 ± 0.008 for the ones fabricated on CuI (Fig. 4c), a difference that is not statistically relevant in this case. Additionally, this analysis shows that CuI-based devices present an overall reproducibility comparable to or better than PEDOT-based devices in the same lab environment, addressing the significant challenge that many alternative HTL materials face (*vide infra*).

To investigate the reasons behind the device improvement, we employed Kelvin-probe force microscopy (KPFM) to extract the surface potential and calculate the Fermi level of each HTL. To ensure reliability, we also extracted the Fermi level of the ITO substrate and the ITO substrate after UV/$O_3$ treatment, as employed before HTL deposition. Our data show that PEDOT:PSS deposited on ITO leads to a Fermi level energy of −4.8 eV, while CuI downshifts it to −5.5 eV, with a small deviation of ± 0.1 eV (Fig. S2). This indicates an expected improvement in energy alignment with the conduction band of our Sn–Pb perovskite (expected at −5.6 eV).[11,43–45] Therefore, a more efficient hole extraction with minimized charge accumulation is expected to occur in the CuI-based solar cells, leading to higher photocurrent.[46]

The charge recombination was further investigated with impedance spectroscopy under open-circuit and dark conditions (Fig. S9). PEDOT:PSS-based devices present two semicircles fitted by two RC components, as shown in Fig. S10. The low-frequency arch describes recombination at the PEDOT:PSS/perovskite interface and the presence of moving ions. The larger high-frequency semicircle is related to the recombination occurring in the perovskite bulk.[47] Specifically, the high-frequency semicircle for both CuI and PEDOT:PSS-based solar cells has been fitted with two RC elements: the first RC element ($CPE_1$–$R_2$) describes recombination in the perovskite layer, while the second RC element ($C_3$–$R_3$) is related to the surface charge accumulation at the HTL/perovskite or ETL/perovskite interfaces.[48,49] Interestingly, CuI-based devices exhibit only the high-frequency arch, indicating a widely reduced ionic motion and interfacial charge trapping. This agrees with the improved energy alignment of CuI with the Sn–Pb perovskite. Mott–Schottky analysis (Fig. S11) reveals a decrease in background charge-carrier density from 8.52 × $10^{15}$ $cm^{-3}$ for PEDOT:PSS to 6.83 × $10^{15}$ $cm^{-3}$ for CuI-based solar cells. The background charge-carrier density is mainly caused by self p-doping due to $Sn^{2+}$ oxidation, which generates Sn vacancies,[39] and indeed, this reduced background charge-carrier density could be one of the reasons for the increased $J_{sc}$.[50]

Furthermore, the iodine-terminated surface of CuI likely promotes chemical compatibility with the perovskite material, contributing to interface passivation and reduced defect density. As discussed in previous publications, CuI may interact with defective perovskite surfaces by supplying iodine to fill halide vacancies and bind metal cations, while its electropositive copper atoms chelate halide anions.[51,52]

In the choice of the HTL in perovskite solar cells, device stability must be carefully considered alongside performance. Given the critical issues associated with PEDOT:PSS, it appears to be of fundamental importance to test the device stability using CuI as the HTL. We therefore investigated the stability of both different device types, looking at their storage lifetime and their stability under high-temperature stress, which is particularly critical for Sn-containing perovskites known to degrade significantly under thermal stress at temperatures as low as ~90 °C, often more severely than under light-induced degradation.[53,54]

As shown in Fig. 5a, we tracked the shelf-life stability in $N_2$ conditions for the two types of devices. The one using CuI as the HTL retained 92.8% of its efficiency after 155 days of testing, while the device using PEDOT:PSS as the HTL exhibited a higher

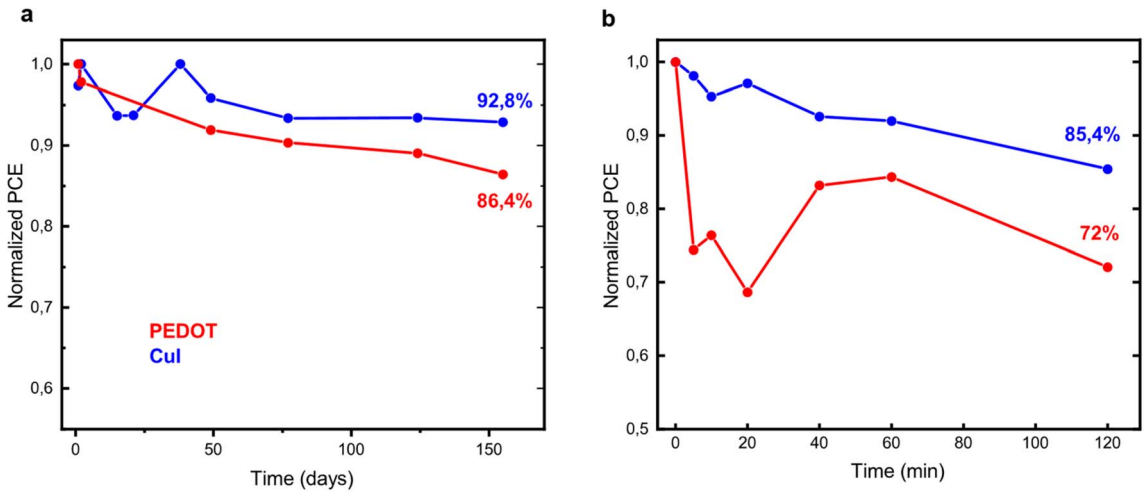


Fig. 5 (a) Shelf-life stability data for unencapsulated devices using PEDOT:PSS (red) and CuI (blue) as HTLs. Devices were stored in a $N_2$ atmosphere under dark conditions. The maximum efficiencies in the plot are 17.69 and 20.03% for the reference device and the one on CuI, respectively. (b) High temperature stability (85 °C in a $N_2$ atmosphere) PCE data for the unencapsulated reference device (red) and the one using CuI HTL (blue).

decay slope reaching after the same number of days 86.4% of the initial PCE. High-temperature stress tests at 85 °C in a $N_2$-filled glovebox (Fig. 5b) further highlight the improved stability of the CuI HTL, which maintained 85.4% of its initial PCE after 120 minutes, compared to 72% for the reference PEDOT:PSS device.

Maximum power point tracking (MPPT) measurements were taken under 1 sun illumination on unencapsulated devices and without using a UV filter. Consistent with our prior observations, CuI-based devices exhibited a smaller initial "burn-in" decay followed by a nearly flat response over subsequent hours, outperforming PEDOT:PSS and indicating superior operational stability (Fig. S12). UV-driven mechanisms on CuI, such as Cu ion migration and defect-chemistry changes, likely accelerate aging.[55,56] Accordingly, the implementation of UV cutoff filters, commonly used in commercial photovoltaic modules, could mitigate these degradation pathways and further enhance the operational stability of CuI-based devices.

Overall, we demonstrate that CuI is a robust HTL for Sn–Pb perovskites, delivering both improved performance and enhanced stability compared to PEDOT:PSS, owing to its improved energy alignment and reduced recombination.

In comparison with the state-of-the-art HTLs such as self-assembled monolayers (SAMs) employed with similar perovskite compositions, the devices reported in this work achieve competitive performance, though with slightly inferior yet comparable thermal stability.[23]

The prospects for this HTL are particularly promising, as CuI can also be doped to further tune and enhance its electrical properties.[24,29,57]

# Conclusions

We demonstrated the successful application of solution-processed CuI as a hole transport layer for the fabrication of Sn–Pb perovskite solar cells using $EACl_{0.015}Cs_{0.25}FA_{0.75}Sn_{0.5}Pb_{0.5}I_3$ as the active layer. A remarkable short circuit current of 32.85 mA $cm^{-2}$ and a power conversion efficiency of 20.1% are obtained for the champion device with CuI, compared to a $J_{sc}$ value of 30.59 mA $cm^{-2}$ and a PCE of 19.03% for the champion device with PEDOT:PSS.

Morphological, optical, and electrical characterizations indicate that perovskite solar cells using CuI as the HTL exhibit reduced defects, show an improved energy alignment between the perovskite and the HTL, and show enhanced charger carrier dynamics with lower non-radiative recombination when compared to devices using PEDOT:PSS as the HTL. Impedance spectroscopy further confirmed lower ionic motion and interfacial charge trapping in devices using CuI than in devices using PEDOT:PSS.

Moreover, devices using CuI show improved stability with respect to the one using PEDOT:PSS, retaining 92.8% of their initial efficiency after 155 days of storage in a nitrogen-filled glovebox. Importantly, CuI-based devices also exhibited superior thermal stability, maintaining better performance after the test at 85 °C.

At the end, we believe that this is only the beginning for CuI, as further improvements are likely through the exploration of alternative deposition techniques and doping strategies aimed at enhancing its conductivity—and consequently, device efficiency.

# Experimental methods

### Materials

Custom patterned ITO substrates (30 × 30 $mm^2$) were directly purchased. Poly(3,4-ethylenedioxythiophene)polystyrene sulfonate (PEDOT:PSS) in a water dispersion (Clevios VP Al 4083) was purchased from Heraeus. Formamidinium iodide (FAI, >98%), ethylamine hydrochloride (>98%) and bathocuproine (BCP, >99%) were bought from TCI EUROPE N. V. Tin(II) iodide ($SnI_2$, 99.99%), tin(II) fluoride ($SnF_2$, 99%), cesium iodide (CsI, 99.999%), dimethylformamide (DMF,99.8%), anisole (anhydrous, 99.7%), copper(I) iodide (CuI, 99.995%), 2,2,2-trifluoroethanol (TFE, >99%), sodium fluoride (NaF, >99%) and buckminsterfullerene (C60, 99.9%) were supplied from Sigma-Aldrich. Lead(II) iodide ($PbI_2$, 99.999%), di-*n*-propyl sulfide (>98%) and dimethyl sulfoxide (DMSO, >99.8%) were acquired from Alfa Aesar/Thermo Scientific. Ag (99.99%) was purchased from Umicore.

### Device fabrication

The ITO patterned glasses were cleaned using soapy water and then sonicated in water, acetone, and 2-propanol. After oven-drying at 140 °C for 30 min, the substrates were treated with UV-ozone for 30 min and, after that, were ready for the HTL deposition.

The CuI solution was prepared at a concentration of 10 mg $mL^{-1}$ in propyl sulfide. CuI was deposited on ITO in a $N_2$-filled glovebox by a spin coating process at 3000 rpm for 30 s and annealed at 100 °C for 3 min. Commercial PEDOT:PSS dispersion was spin-coated at 3000 rpm for 60 s and annealed at 140 °C for 20 min in air. For the CuI-based devices, different deposition conditions were preliminarily investigated, including variations in concentration and the use of acetonitrile as an alternative solvent, as shown in Fig. S13.

The perovskite precursor solution with a concentration of 1.4 M was prepared by dissolving EACl (0.021 mmol), $SnI_2$ (0.7 mmol), FAI (1.05 mmol), CsI (0.35 mmol), $SnI_2$ (0.7 mmol), $PbI_2$ (0.7 mmol) and $SnF_2$ (0.07 mmol) in 800 mL of DMF and 200 mL of DMSO (4 : 1 ratio). The solution was left under stirring for 3 hours (room temperature) and then filtered using 0.2 mm pore size PTFE membrane filters. Next, the perovskite solution was spin-coated on ITO/HTL substrates at 4000 rpm for 70 s in a $N_2$-filled glovebox with $O_2$ and $H_2O$ concentrations <0.1 ppm. Anisole (250 mL) was used as the antisolvent and dropped 25 s after the start of the spin coating program. The perovskite films were annealed at 120 °C for 10 min, immediately at the end of the spin coating deposition. The obtained $EACl_{0.015}Cs_{0.25}FA_{0.75}Sn_{0.5}Pb_{0.5}I_3$ films were passivated with sodium fluoride (NaF) *via* spin-coating at 2000 rpm for 30 s and annealed on a hotplate at 85 °C for 5 min.

 

After that, the samples were moved to a vacuum chamber where 60 nm of C60 and 6 nm of BCP were thermally evaporated at pressures in the order of $10^7$ mbar. Finally, 100 nm of Ag were evaporated on the top of the BCP layer as the metal contact.

### Film and device characterization

X-ray diffraction (XRD) patterns were acquired on CuI films without encapsulation in air using a Bruker D8 Advance X-ray diffractometer with a Cu Ka source ($l = 1.54$ Å) and a Lynxeye detector. Scanning electron microscopy (SEM) was performed using a Nova NanoSEM 650 at an accelerating voltage of 5 kV. Atomic force microscopy (AFM) of the CuI morphology was performed using a Bruker Multimode 8 microscope with ScanAsyst air probes (resonant frequency of 70 kHz and spring constant of 0.4 N $m^{-1}$). The AFM images were recorded at a scan rate of 0.912 Hz with a resolution of 1024 samples per line. Kelvin probe force microscopy (KPFM) measurements were performed using the same Bruker microscope, with SCM-PIT-V2 probes (resonant frequency of 75 kHz and spring constant of 3 N $m^{-1}$) and the electrical & magnetic lift modes/surface potential (FM-KPFM). A freshly cleaved, highly ordered pyrolytic graphite with a work function (WF) of 4.6 eV was used to determine the WF of the tip. Contact angle measurements were performed using a Biolin Scientific Theta Lite instrument in air, with a solvent drop size of 4 µl.

Steady-state and time-resolved photoluminescence (PL) measurements were performed in reflection geometry, exciting the samples from the back side of the ITO/HTL/perovskite film (glass ITO side). An excitation wavelength of 400 nm was obtained as the second harmonic of a mode-locked Ti : sapphire laser (Coherent Mira 900). The laser repetition rate of 76 MHz was reduced through an optical pulse picker to extend the time range in the time-resolved measurements. Steady-state spectra were acquired using a Hamamatsu spectral-calibrated EM-CCD camera. Time-resolved PL traces were taken using a Hamamatsu streak camera working in a single-sweep mode. The samples were mounted in a sealed sample holder and kept in a $N_2$ atmosphere during the measurements.

The absorption spectrum of the ITO/HTL films was acquired using a Shimadzu UV-vis-NIR spectrophotometer (UV 3600).

The *J–V* characteristics of the solar cells were measured in a nitrogen-filled glovebox ($O_2$ < 0.1 ppm and $H_2O$ < 0.1 ppm) under standard test conditions (295 K, AM1.5G solar illumination) using a Keithley 2400 source meter and a Steuernagel Solar constant 1200 metal halide lamp.

The system was calibrated using a Si reference cell. A shadow mask (0.04 $cm^2$) was used to exclude contributions outside the device area. A home-built setup was used for measuring the external quantum efficiency (EQE) of the solar cells, in which a set of filter wheels allowed measurements in the spectral range of 400–1400 nm. The samples were mounted in a sealed sample holder and kept in a $N_2$ atmosphere during the measurements.

The measured simulator spectrum was compared with the AM1.5G reference, and the spectral mismatch factor (M) was computed using the EQE of a test cell and that of a calibrated silicon reference cell. The standard energy-responsivity formulation (equivalent to the photon–EQE form) was used, where with spectral irradiance $E(\lambda)$ and spectral responsivity $SR(\lambda)$, the factor is

$$M = \frac{\int E_{AM\ 1.5}(\lambda)SR_{RefCell}(\lambda)d\lambda}{\int E_{AM\ 1.5}(\lambda)SR_{TestCell}(\lambda)d\lambda} \cdot \frac{\int E_{Lamp}(\lambda)SR_{TestCell}(\lambda)d\lambda}{\int E_{Lamp}(\lambda)SR_{RefCell}(\lambda)d\lambda}$$

The calculated $M$ for the reported cells is 1.08, indicating that approximately 8% of the observed $J_{sc}$ discrepancy arises from spectral mismatch.

The photocurrent was measured using a lock-in amplifier (Stanford Research Systems, Model SR830 DSP Lock-In Amplifier). To calibrate the photon flux, a set of calibrated Newport optical power detectors (Newport Model 818-SL and Model 818-IR) were used.

Capacitance–voltage (*C–V*) measurements were performed using a Solartron 1260 impedance gain-phase analyzer. The measurements were conducted under dark conditions, applying an AC drive voltage with an amplitude of 10 mV and a frequency of 10 kHz. The applied DC bias was swept across the range of −0.8 V to 0.8 V. For impedance spectroscopy, the frequency was swept from 0.1 Hz to 1 MHz, while the device was kept under open-circuit conditions.

## Conflicts of interest

The authors declare no conflict of interest.

## Data availability

Data are available from the authors upon request.

Supplementary Information is available. See DOI: https://doi.org/10.1039/d5ta06770g.

## Acknowledgements

We kindly acknowledge A. Kamp and T. Zaharia for technical support. This publication is part of the Netherlands Organization for Scientific Research (NWO)'s focus Group “Next Generation Organic Photovoltaics”, participating in the Dutch Institute for Fundamental Energy Research (DIFFER). This work was partially funded by the European Union's Horizon 2020 program, through a FET Proactive research and innovation action under grant agreement No. 101084124 (DIAMOND). R. P acknowledges PRIN 2022 CUP F53D23005090006 and PRIN 2022 F53D23001050006, funded by Italian Ministry for University and Research (MUR). M. S. acknowledges Project “Network 4 Energy Sustainable Transition—NEST”, Spoke 1, Project code PE0000021, funded under the National Recovery and Resilience Plan (NRRP), Mission 4, Component 2, Investment 1.3 – MUR funded by the European Union—NextGenerationEU.

## References

1 M. A. Green, E. D. Dunlop, M. Yoshita, N. Kopidakis, K. Bothe, G. Siefer, D. Hinken, M. Rauer, J. Hohl-Ebinger and X. Hao, *Prog. Photovoltaics Res. Appl.*, 2024, **32**, 425.
2 J. Li, H.-L. Cao, W.-B. Jiao, Q. Wang, M. Wei, I. Cantone, J. Lü and A. Abate, *Nat. Commun.*, 2020, **11**, 310.
3 D. He, P. Chen, J. A. Steele, Z. Wang, H. Xu, M. Zhang, S. Ding, C. Zhang, T. Lin, F. Kremer, H. Xu, M. Hao and L. Wang, *Nat. Nanotechnol.*, 2025, **20**, 779–786.
4 Y. Zhang, C. Li, H. Zhao, Z. Yu, X. Tang, J. Zhang, Z. Chen, J. Zeng, P. Zhang, L. Han and H. Chen, *Nat. Commun.*, 2024, **15**, 6887.
5 S. Kahmann, O. Nazarenko, S. Shao, O. Hordiichuk, M. Kepenekian, J. Even, M. V. Kovalenko, G. R. Blake and M. A. Loi, *ACS Energy Lett.*, 2020, **5**, 2512.
6 S. Kahmann, Z. Chen, O. Hordiichuk, O. Nazarenko, S. Shao, M. V. Kovalenko, G. R. Blake, S. Tao and M. A. Loi, *ACS Appl. Mater. Interfaces*, 2022, **14**, 34253.
7 T. Leijtens, K. A. Bush, R. Prasanna and M. D. McGehee, *Nat. Energy*, 2018, **3**, 828.
8 J. Lim, N. G. Park, S. Il Seok and M. Saliba, *Energy Environ. Sci.*, 2024, **17**, 4390.
9 A. Filippetti, S. Kahmann, C. Caddeo, A. Mattoni, M. Saba, A. Bosin and M. A. Loi, *J. Mater. Chem. A*, 2021, **9**, 11812.
10 T. Leijtens, R. Prasanna, A. Gold-Parker, M. F. Toney and M. D. McGehee, *ACS Energy Lett.*, 2017, **2**, 2159.
11 J. Xi and M. A. Loi, *ACS Energy Lett.*, 2021, **6**, 1803.
12 J. Liang, T. Li, B. Li, Y. Yang, Z. Jin, Z. Zhang, P. Wang, L. Deng, Y. Zhan and Q. Zhang, *Nat. Commun.*, 2024, **1**, 9435.
13 N. K. Noel, S. D. Stranks, A. Abate, C. Wehrenfennig, S. Guarnera, A. A. Haghighirad, A. Sadhanala, G. E. Eperon, S. K. Pathak, M. B. Johnston, A. Petrozza, L. M. Herz and H. J. Snaith, *Energy Environ. Sci.*, 2014, **7**, 3061.
14 F. Hao, C. C. Stoumpos, D. H. Cao, R. P. H. Chang and M. G. Kanatzidis, *Nat. Photonics*, 2014, **8**, 489.
15 N. Sun, W. Gao, H. Dong, Y. Liu, X. Liu, Z. Wu, L. Song, C. Ran and Y. Chen, *ACS Energy Lett.*, 2021, **6**, 2863.
16 V. M. Goldschmidt, *Naturwissenschaften*, 1926, **14**, 477.
17 S. Hu, K. Otsuka, R. Murdey, T. Nakamura, M. A. Truong, T. Yamada, T. Handa, K. Matsuda, K. Nakano, A. Sato, K. Marumoto, K. Tajima, Y. Kanemitsu and A. Wakamiya, *Energy Environ. Sci.*, 2022, **15**, 2096–2107.
18 S. Shao, Y. Cui, H. Duim, X. Qiu, J. Dong, G. H. ten Brink, G. Portale, R. C. Chiechi, S. Zhang, J. Hou and M. A. Loi, *Adv. Mater.*, 2018, **30**, 1803703.
19 F. Hou, Z. Su, F. Jin, X. Yan, L. Wang, H. Zhao, J. Zhu, B. Chu and W. Li, *Nanoscale*, 2015, **7**, 9427.
20 J. C. Yu, J. A. Hong, E. D. Jung, D. Bin Kim, S. M. Baek, S. Lee, S. Cho, S. S. Park, K. J. Choi and M. H. Song, *Sci. Rep.*, 2018, **8**, 3.
21 J. Werner, T. Moot, T. A. Gossett, I. E. Gould, A. F. Palmstrom, E. J. Wolf, C. C. Boyd, M. F. A. M. Van Hest, J. M. Luther, J. J. Berry and M. D. McGehee, *ACS Energy Lett.*, 2020, **5**, 1215.
22 M. Pitaro, J. E. S. Alonso, L. Di Mario, D. G. Romero, K. Tran, J. Kardula, T. Zaharia, M. B. Johansson, E. M. J. Johansson, R. C. Chiechi and M. A. Loi, *Adv. Funct. Mater.*, 2023, **2306571**, 1.
23 M. Pitaro, J. S. Alonso, L. Di Mario, D. Garcia Romero, K. Tran, T. Zaharia, M. B. Johansson, E. M. J. Johansson and M. A. Loi, *J. Mater. Chem. A*, 2023, **11**, 11755.
24 C. Yang, M. Kneib, M. Lorenz and M. Grundmann, *Proc. Natl. Acad. Sci. U. S. A.*, 2016, **113**, 12929.
25 A. Liu, H. Zhu, W. T. Park, S. J. Kang, Y. Xu, M. G. Kim and Y. Y. Noh, *Adv. Mater.*, 2018, **30**, 1.
26 K. Bädeker, *Ann. Phys.*, 1907, **327**, 749.
27 M. Grundmann, F. L. Schein, M. Lorenz, T. Böntgen, J. Lenzner and H. Von Wenckstern, *Phys. Status Solidi Appl. Mater. Sci.*, 2013, **210**, 1671.
28 B. L. Zhu and X. Z. Zhao, *Phys. Status Solidi Appl. Mater. Sci.*, 2011, **208**, 91.
29 K. Ahn, G. H. Kim, S. J. Kim, J. Kim, G. S. Ryu, P. Lee, B. Ryu, J. Y. Cho, Y. H. Kim, J. Kang, H. Kim, Y. Y. Noh and M. G. Kim, *Chem. Mater.*, 2022, **34**, 10517.
30 K. Zhao, G. O. Ngongang Ndjawa, L. K. Jagadamma, A. El Labban, H. Hu, Q. Wang, R. Li, M. Abdelsamie, P. M. Beaujuge and A. Amassian, *Nano Energy*, 2015, **16**, 458.
31 C. H. Choi, J. Y. Gorecki, Z. Fang, M. Allen, S. Li, L. Y. Lin, C. C. Cheng and C. H. Chang, *J. Mater. Chem. C*, 2016, **4**, 10309.
32 S. Inudo, M. Miyake and T. Hirato, *Phys. Status Solidi Appl. Mater. Sci.*, 2013, **210**, 2395.
33 W. Y. Chen, L. L. Deng, S. M. Dai, X. Wang, C. B. Tian, X. X. Zhan, S. Y. Xie, R. Bin Huang and L. S. Zheng, *J. Mater. Chem. A*, 2015, **3**, 19353.
34 W. Sun, S. Ye, H. Rao, Y. Li, Z. Liu, L. Xiao, Z. Chen, Z. Bian and C. Huang, *Nanoscale*, 2016, **8**, 15954.
35 T. Prakash, *Adv. Mater. Lett.*, 2011, **2**, 131.
36 N. Yamada, R. Ino and Y. Ninomiya, *Chem. Mater.*, 2016, **28**, 4971.
37 K. M. Archana, D. Yogalakshmi and R. Rajagopal, *SN Appl. Sci.*, 2019, **1**, 1.
38 E. Smith and D. Venkataraman, *Chempluschem*, 2022, **87**, e202200101.
39 S. Kahmann, S. Shao and M. A. Loi, *Adv. Funct. Mater.*, 2019, **29**, 1.
40 S. Shao, J. Dong, H. Duim, G. H. ten Brink, G. R. Blake, G. Portale and M. A. Loi, *Nano Energy*, 2019, **60**, 810.
41 Y. Huang, Y. Jiang, S. Zou, Z. Zhang, J. Jin, R. He, W. Hu, S. Ren and D. Zhao, *ACS Appl. Mater. Interfaces*, 2023, **15**, 15775.
42 K. Nishimura, M. A. Kamarudin, D. Hirotani, K. Hamada, Q. Shen, S. Iikubo, T. Minemoto, K. Yoshino and S. Hayase, *Nano Energy*, 2020, **74**, 104858.
43 J. Cao, C. ki Liu, Y. Xu, H. L. Loi, T. Wang, M. G. Li, L. Liu and F. Yan, *Small*, 2024, (1), 2403920.
44 F. Hao, C. C. Stoumpos, R. P. H. Chang and M. G. Kanatzidis, *J. Am. Chem. Soc.*, 2014, **136**, 8094.
45 M. Pitaro, J. S. Alonso, L. Di Mario, D. Garcia Romero, K. Tran, T. Zaharia, M. B. Johansson, E. M. J. Johansson and M. A. Loi, *J. Mater. Chem. A*, 2023, **11**, 11755.

46 X. Shi, K. Xu, Y. He, Z. Peng, X. Meng, F. Wan, Y. Zhang, Q. Guo and Y. Chen, *Nano-Micro Lett.*, 2025, **17**, 313.
47 E. Von Hauff and D. Klotz, *J. Mater. Chem. C*, 2022, **10**, 742.
48 I. Zarazúa, S. Sidhik, T. Lopéz-Luke, D. Esparza, E. De La Rosa, J. Reyes-Gomez, I. Mora-Seró and G. Garcia-Belmonte, *J. Phys. Chem. Lett.*, 2017, **8**, 6073.
49 I. Zarazua, G. Han, P. P. Boix, S. Mhaisalkar, F. Fabregat-Santiago, I. Mora-Seró, J. Bisquert and G. Garcia-Belmonte, *J. Phys. Chem. Lett.*, 2016, **7**, 5105.
50 M. A. Karim, K. Matsuishi, M. E. Kayesh, Y. He and A. Islam, *ACS Appl. Mater. Interfaces*, 2023, **15**, 45823.
51 S. Ye, H. Rao, Z. Zhao, L. Zhang, H. Bao, W. Sun, Y. Li, F. Gu, J. Wang, Z. Liu, Z. Bian and C. Huang, *J. Am. Chem. Soc.*, 2017, **139**, 7504.
52 D. Saranin, P. Gostischev, D. Tatarinov, I. Ermanova, V. Mazov, D. Muratov, A. Tameev, D. Kuznetsov, S. Didenko and A. Di Carlo, *Mater.*, 2019, **12**, 1.
53 A. F. Akbulatov, S. A. Tsarev, M. Elshobaki, S. Y. Luchkin, I. S. Zhidkov, E. Z. Kurmaev, S. M. Aldoshin, K. J. Stevenson and P. A. Troshin, *J. Phys. Chem. C*, 2019, **123**, 26862.
54 L. Chen, S. Fu, Y. Li, N. Sun, Y. Yan and Z. Song, *Adv. Sci.*, 2024, **11**, 1.
55 Y. Zhang, L. Liu, Z. Wang, Y. Yang and F. Xing, *J. Alloys Compd.*, 2022, **900**, 163456.
56 T. M. Kim, J. W. Kim, H. S. Shim and J. J. Kim, *Appl. Phys. Lett.*, 2012, **101**, 113301.
57 A. S. Mirza, M. Pols, W. Soltanpoor, S. Tao, G. Brocks and M. Morales-Masis, *Matter*, 2023, **6**, 4306.